I radio galaxies derived combining available samples (see Pesce 1993) yields $<N_{0.5}>_{FRI} = 7.1 \pm 8$. The large scatter being due in part to differences of samples and redshift distribution.

We note also that F-R I radio galaxies represent an heterogeneous class and it is possible that the parent objects of BL Lacs form a subset of F-R I galaxies.

Objects in our sample are a mixture of radio selected and X-ray selected targets (corresponding to radio-strong and radio-weak emitters). Although a number of different emission properties are found to characterize these subclasses (see e.g. Giommi *et al.* 1994), we do not find systematic differences of environment between the two.

Our results are consistent with what is being found by other similar studies. Wurtz *et al.* (1993) and Smith *et al.* (1995) have concentrated on X-ray selected BL Lac objects while Stickel *et al.* (1993) and Fried *et al.* (1993) have studied some of the radio selected BL Lacs. In most cases, the clusters found are relatively poor (Abell richness class 0-1) with a few objects in richer environments.

If BL Lacs are aligned versions of low-luminosity (F-R I) radio galaxies, it might be expected that Flat Spectrum Radio Quasars (FSRQs), which share many of the properties of BL Lacs but have strong and broad emission lines, are aligned examples of high-luminosity (F-R II) radio galaxies. We point out that a detailed comparison of environmental and host properties of BL Lacs and F-R I galaxies with FSRQs and F-R II radio galaxies would help to constrain the proposed unified schemes of AGN.

Acknowledgement

We thank A. Treves for useful suggestions to this manuscript. J.E.P. and work on BL Lac environments at STScI are supported by NASA grants NAG5-1034 and NAG5-2154.

References

Abell, G. O., 1958, *ApJS*, **3**, 211.
Angel, J. R. P., & Stockman, H. S., 1980, *ARAA*, **18**, 321.
Bahcall, N. A. 1981, *ApJ*, **247**, 787.
Blandford, R. D., & Rees, M. J. 1978, in Pitts. Conference on BL Lac Objects, ed. A. N. Wolfe (Univ. of Pitts. Press), 328.
Bregman, J. P., 1990, *A&AR*, **2**, 125.
Browne, I. W. A. 1983, *MNRAS*, **204**, 23.
Butcher, H. R., *et al.* 1976, *ApJ*, **209**, L11.
Craine, E. R., Tapia, S., & Tarenghi, M., 1975, *Nature*, **258**, 56.
Disney, M. J., 1974, *ApJL*, **193**, L103.
Falomo, R., Pesce, J. E., & Treves, A., 1993, *AJ*, **105**, 2031.
Falomo, R., Pesce, J. E., & Treves, A. 1994, *ApJ Letters*, in press.
Falomo, R., & Tanzi, E. G., 1991, *AJ*, **102**, 1294.
Falomo, R., Tanzi, E. G., & Treves, A., 1991, *A&A*, **249**, 341.
Fosbury, R. A. E., & Disney, M. J., 1976, *ApJL*, **207**, L75.
Fried, J. W., Stickel, M., & Kühr, H., 1993, *A&A*, **268**, 53.
Giommi, P., *et al.* 1991, *ApJ*, **378**, 77.
Giommi, P., Ansari, S. and Micol, A. 1994, *A&ASS*, in press.
Hartwick, F.D.A. and Schade, D. 1990, *Ann. Rev. Astr. Astrophys.* **28**, 437.
Hartman, R., *et al.* 1993, in Proc. of the 2nd Compton Symposium, College Park, MD, Sept. 1993, in press.
Hill, G. J., & Lilly, S. J., 1991, *ApJ*, **367**, 1.
Hintzen, P., Romanishin, W., & Valdes, F., 1991, *ApJ*, **366**, 7.
Jarvis, J. F., & Tyson, J. A., 1981, *AJ*, **86**, 476.
Kollgaard, R. I., *et al.* 1992, *AJ*, **104**, 1687.
Kollgaard, R. I 1994, *Vistas in Astronomy*, **38**, 29.
Maraschi, L., Ghisellini, G., & Celotti, A., 1992, *ApJ*, **397**, L5.
M^{c}Hardy, I. M., Luppino, G. A., George, I. M., Abraham, R. G., & Cooke, B. A., 1992, *MNRAS*, **256**, 655.
Metcalfe, N., Shanks, T., Fong, R., & Jones, L. R., 1991, *MNRAS*, **249**, 498.
Pesce, J. E 1993, PhD Thesis.
Prestage, R. M., & Peacock, J. A., 1988, *MNRAS*, **230**, 131.
Prestage, R. M., & Peacock, J. A., 1989, *MNRAS*, **236**, 959.
Schachter, J. F., *et al.* 1993 *ApJ*, **412**, 541.
Smith, E. P., O'Dea, C. P., & Baum, S. A., 1995, *ApJ*, in press.
Stickel, M., *et al.* 1991, *ApJ*, **374**, 431.
Stickel, M., Fried, J. W., & Kühr, H. 1993, A&AS, 98, 393.
Stocke, J. T., *et al.* 1991, *ApJS*, **76**, 813.
Stone, R. P. S., 1977, *ApJ*, **218**, 767.
Treves, A., *et al.* 1989, *ApJ*, **341**, 733.
Ulrich, M.-H. 1978, *ApJ*, **222**, L3.
Urry, C. M., Padovani, P., & Stickel, M. 1991, *ApJ*, **382**, 501.
Weistrop, D., *et al.* 1981, *ApJ*, **249**, 3.
Wurtz, R., Ellingson, E., Stocke, J. T., & Yee, H. K. C., 1993, *AJ*, **106**, 869.
Yates, M. G., Miller, L., & Peacock, J. A., 1989, *MNRAS*, **240**, 129.

COME-ON+ Adaptive Optics Images of the Pre-Main Sequence Binary NX Pup

E. TESSIER[1], *J. BOUVIER*[2], *J.-L. BEUZIT*[3,5] *and W. BRANDNER*[4,5]

[1]*Royal Greenwich Observatory, Cambridge, England;* [2]*Observatoire de Grenoble, Université Joseph Fourier, France;* [3]*Observatoire de Paris, Section de Meudon, France;* [4]*Astronomisches Institut der Universität Würzburg, Germany;* [5]*ESO-La Silla*

Introduction

Using adaptive optics (AO) at the ESO 3.6-m telescope, we obtained diffraction limited JHK images of the region around the Herbig AeBe star NX Pup. NX Pup is resolved as a close binary with a separation of 0.128″ (the binary nature of NX Pup was originally discovered by HST) that we refer to as NX Pup AB; a third component NX Pup C is found at a distance of 7.0″ and is classified as a classical T Tauri star. We first describe the procedure that we followed in order to extract the maximum information from the AO images. We then discuss the evolutionary status of the NX Pup system on the basis of its IR properties derived from the AO images, as well as from the visual photometry and spectroscopy subsequently obtained at ESO.

AO Observations

We used the ESO adaptive optics system ComeOn+ (CO+), which was developed in collaboration by the Observatoire de Paris, ONERA, ESO, Laserdot and LEP, in combination with the SHARP II (System for High Angular Resolution Pictures) camera from the Max-Planck Institute for Extraterrestrial Physics (MPE). See Beuzit *et al.* 1994, *The Messenger* 75, 33 and references therein for a description of the CO+ system. The SHARP II camera is equipped with a Rockwell NICMOS-3 array. The image scale was 0.050″/pixel giving a field size of 13″× 13″. We observed NX Pup on

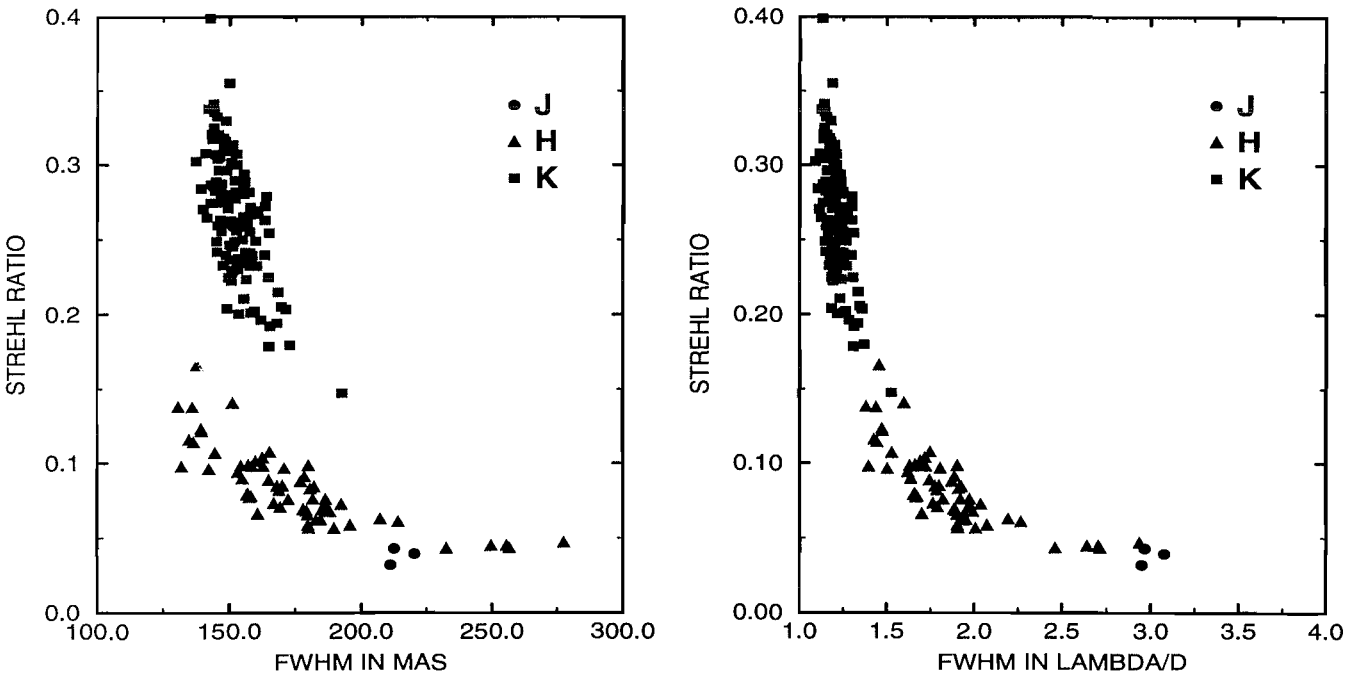

Figure 1: *Plot of FWHM versus Strehl ratio (SR) for individual images obtained with the Adaptive Optics system Come-On+. The exposure time was 1s in HK and 20 s in J. In K, the FWHM is well stabilized, and always better than 0.18″. The scatter in the HK points shows that short individual images are influenced by the continuous change of the turbulence conditions due to the short coherence time of the turbulence during that night. For longer exposure times, these effects average out as shown by the small scatter of the three 20 s images in J. Note that the narrower diffraction core in H allows better FWHM than in K for some images in spite of a lower SR. The same plot is rescaled by λ/D on the right (which is the diffraction limit) to show the relation between FWHM and SR which characterizes AO images. This curve is valid for the Come-On+ experiment.*

January 1, 1994 in the J, H, and K bands. The total exposure time in each filter was 5 minutes. Immediately after NX Pup, we observed a reference point source 10′ away (star no. 985 in the HST Guide Star Catalogue) later used to measure the instrumental point spread function (PSF) which is necessary to deconvolve images; we will refer to it as the calibration PSF source. The guide source used by the AO system was in both cases the observed source itself. Since NX Pup is a rather bright source (around 6th mag in K) and the calibration source is selected to match the same flux, we obtained series of short exposures in the H and K band (respectively 0.5 s and 2 s for NX Pup) in order to fall in the linear response region of the detector. Because NX Pup is fainter in J and because of the lower sensitivity of the detector in this wavelength region, the exposure time in J was 1 minute in each frame for NX Pup. We therefore have a large number of individual exposures in the H and K bands and we will show below how we can take advantage of it.

Characterization of AO Images

Since an AO system partially or fully compensates the wavefront distorsions, we now have access to imaging with a point spread function much sharper than the seeing disk. The shape of the PSF could be described as a diffraction-limited core superimposed on a residual halo with a size corresponding approximatively to the seeing disk. This halo comes from the high-order Zernike modes not corrected by the Adaptive Optics system. The diffraction-limited core may be wider (we can represent this by a Gaussian convolution) when errors of correction for the low-order Zernike modes are important. The performance of an AO system at any wavelength is usually defined by the Strehl ratio (SR). The Strehl ratio is the ratio of the observed PSF maximum to the theoretical diffraction-limited PSF maximum; the latter is the Airy pattern for a clear circular aperture telescope of diameter D. When the SR increases, the halo size will reduce and its power will move to the diffraction limited core (see Rigaut *et al.* 1991).

Consequently the image obtained is that of the source convolved with the instrumental PSF and image deconvolution may therefore be needed (particularly to clearly access structures superimposed on the PSF patterns such as the first Airy ring or the residual seeing halo). The PSF may be calibrated on a point source in similar seeing conditions. We will talk about a deconvolution procedure in a next section.

Figure 1 shows the distribution of the full width half maximum (FWHM) versus Strehl ratio (SR) for each individual exposures of the calibration PSF in JHK. The exposure time was 1 s in HK bands, 20 s in J. We can see that the image in the K band is very well stabilized, FWHM being always less than 0.18″. In H, the SR drops below 10%, a key value below which the correction is much more sensitive to turbulence effects as shown by the large variations of the FWHM between 0.13″ and 0.25″. The distribution of the points in the HK-bands illustrates how the PSF varies as the turbulence conditions continuously change during the observations. The scatter of the points depends upon the coherence time of the turbulence: had the coherence time been longer that night, the PSF would have been much less sensitive to varying turbulence conditions. As a rule, the worst the turbulence, the less efficient the correction. The PSF variation in response to the changing turbulence is reduced with longer exposure times and/or by coadding individual images. This is why the scatter of the 3 images in J is much reduced due to the exposure time of 20 s compared with 1s for the HK bands (see Fig.1).

When the plot abscissa is rescaled by a factor λ/D (which corresponds to the diffraction limit at the wavelength λ for a telescope of diameter D), points clearly gather along a single curve. As shown by this curve, the Strehl ratio describes

very well the PSF with a SR above 10% but poorly for lower values. In the latter case, the FWHM will provide additional information on the PSF.

This curve is valid for the ComeOn+ experiment and characterizes the PSF response. Other AO systems may give different responses. Anyway, these plots could be used to define the best strategy in AO observing. As a rule, the turbulence effects get worse as one goes to shorter wavelengths; consequently, the correction and the SR are poorer. However, in some cases, by going to shorter wavelengths one can get higher resolution in spite of a lower SR; this is because the FWHM becomes sharper thanks to the narrower diffraction core (following a λ/D law). For example, in the observation of NX Pup, in terms of FWHM, the best individual images are in the H-band rather than in the K-band (see Fig. 1).

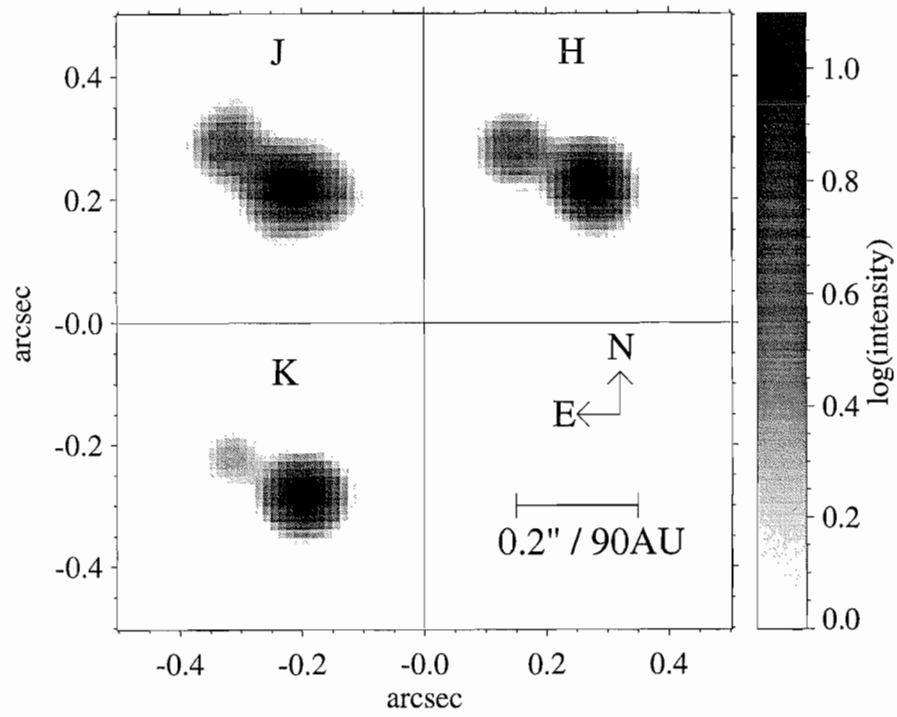

Figure 2: *Cleaned images of NX Pup AB obtained in JHK with the Adaptative Optics system CO+ at the ESO 3.6-m telescope on January 1, 1994. The images were rebinned by a factor of 4, the FWHM of the Gaussian beam is 80 mas (see text for details). The components A and B (sep. 0.128″, PA 63.1°) are clearly resolved. At a distance of 450 pc, 0.128″ correspond to a projected separation of 58 AU. The faint feature in the J image north-west of NX Pup A is an artefact from the image deconvolution. A logarithmic gray scale was used. Component C is outside these frames. North is up and east is to the left.*

Sharpening Methods for Short-Exposure AO Images

The number of individual exposures on NX Pup was 5 in J, 150 in H, and 600 in K for a total exposure time of 300 seconds in each filter.

A simple coaddition of these individual frames yields the final image. However, when a large amount of images is available, it is worth selecting them according to a Strehl ratio criterium. Also, when a short exposure time is used, the residual tilt is further reduced by applying a shift-and-add algorithm (SAA).

While SAA mostly improves the resulting FWHM, applying image selection increases the final Strehl ratio. However, the rejection rate of images with poor SR must be limited in order to preserve a large enough signal-to-noise ratio in the final image. Table 1 quantitatively shows the improvement on the calibration PSF obtained with image selection (IS) and SAA in comparison to the simple coaddition of individual frames. The number of individual exposures on the calibration PSF source was 3 in J, 60 in H, and 120 in K for a total exposure time of 60 s in JH and 120 s in K. All these operations were performed with the local IRAF package c128 developed by E. Tessier at the Observatory of Grenoble (available through anonymous FTP at the site hplyot.obspm.fr in the directory /iraf_hra).

TABLE 1. *Sharpening result from short exposure AO images through shift and add (SAA) and image selection (IS).*

	J	H	K
FWHM	0.214″	0.172″	0.156″
FWHM (SAA)	0.209″	0.157″	0.147″
FWHM(SAA+IS)	–	0.138″	0.143″
SR	3.8%	8.0%	25.1%
SR (SAA)	3.8%	8.6%	27.1%
SR (SAA + IS)	–	12.4%	31.0%
Selection rate (IS)	–	20%	40%

NX Pup AB: CLEANed AO Images

A simple coaddition of the individual images allows already to resolve the NX Pup AB system with a separation of 0.128″; and this shows how efficient AO imaging is. Nevertheless, even sharper angular resolution can be reached by applying CLEAN deconvolution to the data. We briefly describe here the CLEAN algorithm we used (see also Tessier *et al.* 1993). Using the terms common among radio astronomers, the (SAA+IS) image of the source provides the "dirty map", while that of the calibration PSF is used as the "dirty beam". Both maps are apodized to reject non-physical spatial frequencies beyond the effective cut-off. Then they are resampled by a factor 4 and convolved with a Gaussian beam before running the CLEAN algorithm with a loop gain of 3%. Because we first try to detect close stellar sources and not low-level extended structures, it is important to control the formation of ghost sources and consequently it is better to stop the CLEAN process as soon as the level of the negatives in the Cleaned map reach the level of the residues in the residual map. Usually, for 256×256 maps, convergence is reached in less than 500 iterations. The Cleaned map is then convolved with the same Gaussian beam as used previously and the residuals map is added to get the final Cleaned image.

As a rule, low-level extended structures require that we run the CLEAN algorithm until the noise level is reached. By the way, Maximum Entropy Methods (MEM) are known to be more efficient when dealing with extended structures. Another way to study the presence of extended structures is via analysis in the Fourier space (see Malbet *et al.* 1993). From this analysis, NX Pup AB does not show any significant deviation from the

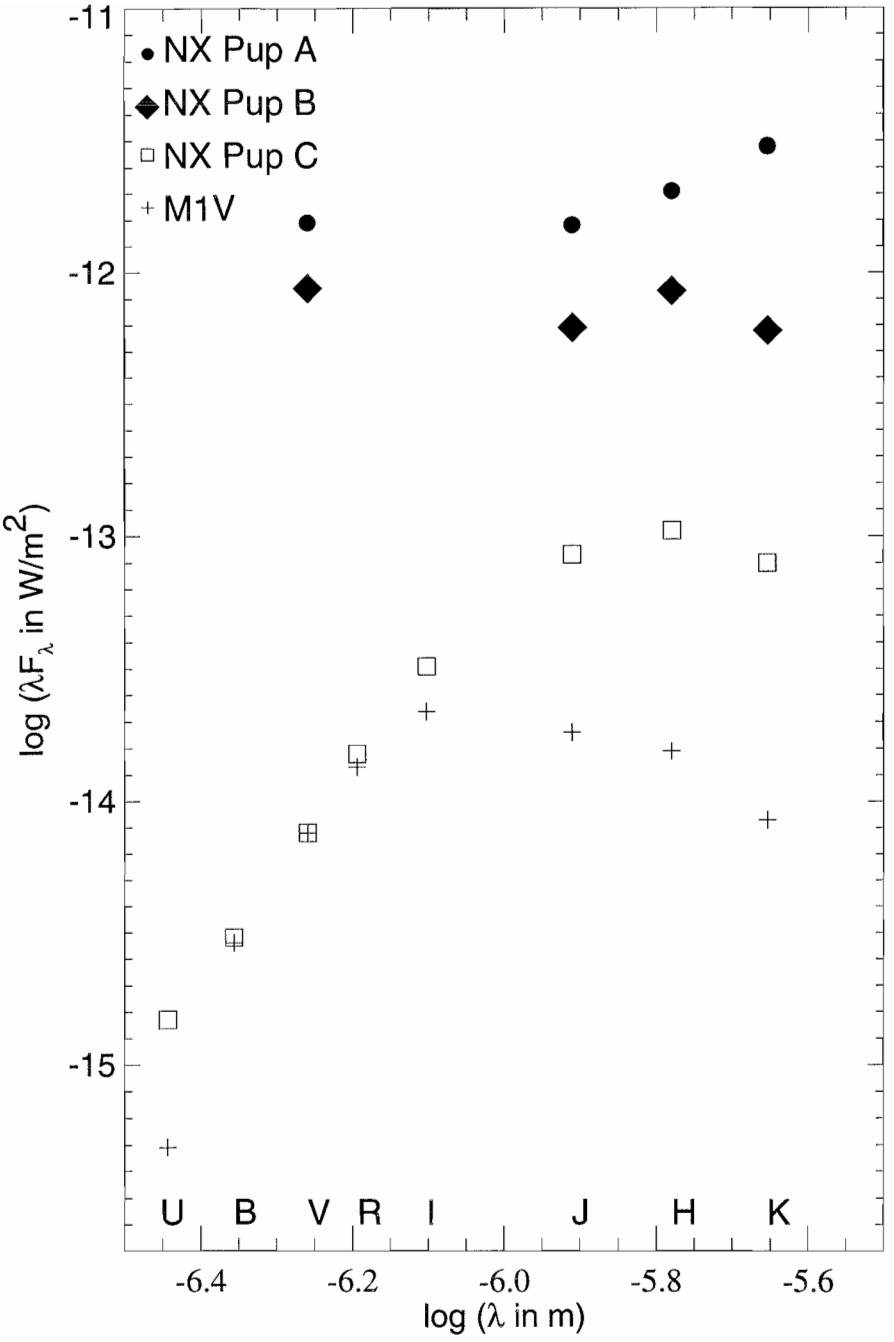

Figure 3: *Spectral energy distribution λ F_λ of NX Pup A and B (VJHK) and C(UBVRIJHK). For comparison we also show the spectral energy distribution of an M1-type star of the same apparent V magnitude as NX Pup C. Note that the SED is rising towards longer wavelengths for NX Pup A while the SEDs of NX Pup B and C peak near 1.5 μm. All 3 stars exhibit a strong IR excess compared to normal photospheres and NX Pup C also shows an UV excess. The errors in flux are 5% or less.*

binary model in the HK bands (the quality of J data is inadequate to confirm this), consequently no other features are detected.

Astrometry of the system was performed on Cleaned images which are shown in Figure 2. The FWHM of the Gaussian beam was 80 mas. Residues in % of the peak value were 8%, 4%, and 1% in JHK, respectively. The separation of 0.128″ ± 0.008″ and the position angle of 63.1° ± 3.5° are in good agreement with the values determined by Bernacca *et al.* (1993) from HST observations: 0.126″ ± 0.007″, 63.4° ± 1.0°.

The total flux is conserved by the CLEAN algorithm. However, though the Cleaned PSF has a sharper peak, it is surrounded by a residual pattern made of positive and negative values due to the noise and to uncertainties in the calibration PSF (incidentally, some features in the Cleaned images of NX Pup located on the first Airy ring are probably artefacts connected with some intensity variations of the PSF in this region – see Figure 2). For that reason, we prefer not to rely on peak values in the Cleaned images to derive photometry. Instead, the photometry was performed on the shift-and-add images using IRAF/DAOPHOT routines. These routines can be compared with a basic blind deconvolution-like process using the calibration PSF only in the first iteration and assuming the source is a binary, which provides a very strong constraint. By doing this, we avoid the calibration PSF problem.

NX Pup C: Off-Axis Sources and Anisoplanatism

NX Pup C is located 7″ away from NX Pup AB. Since the wavefront correction used NX Pup AB as a guide source, NX Pup C is off-axis and image correction might therefore suffer from anisoplanatic effects. Anisoplanatism refers to the case where the distorted wavefront of the observed source (the astronomical target) is different from that of the guide source used by the AO system. As a result, the adaptive correction on the target is degraded. Various types of anisoplanatism affect current AO systems; some ideas, such as using multiple laser beacons, would overcome this limitation (Beckers *et al.* 1993). At the moment, CO+ uses a natural guide star which can be the target itself or a nearby star. We briefly describe below two kinds of anisoplanatism that might result from this observing mode: angular anisoplanatism and temporal anisoplanatism.

If we observe an off-axis source, the telescope is viewing to a direction making an angle θ with the direction of the guide source used by the AO instrument. The light path across the turbulence layers and, therefore, the induced phase perturbations are different for the on- and off-axis sources. The adaptive-optics correction is consequently less efficient for the off-axis source. This direction-dependent anisoplanatism is usually called angular anisoplanatism.

Because the bandwidth B of any AO instrument transfer function is finite, the correction applied at the time t is based on a perturbed wavefront recorded at a time $t - \delta t$. According to the approximation of frozen turbulence, the degradation of the correction is then related to the ratio $\overline{V}/B$, where the wind speed V of the turbulent layers is mainly responsible for the continuous change of the perturbed wavefront. This anisoplanatism is usually called temporal anisoplanatism.

Observations have recently been carried out at the ESO 3.6-m telescope to study the anisoplanatism, and more observations are scheduled in January 1995 (M. Faucherre, private communi-

TABLE 2. *JHK photometry (1.1.1994, ESO 3.6-m/CO+).*

Filter	NX Pup A	NX Pup B	NX Pup C
J	8.58^m	9.56^m	11.71^m
H	7.43^m	8.37^m	10.66^m
K	6.15^m	7.90^m	10.10^m

cation). As long as the final results of these observations are not available, it is therefore difficult to estimate whether angular anisoplanatism is important under good seeing conditions in the case of NX Pup C, 7″ away from the guide source NX Pup AB. Because we might expect some angular anisoplanatism effects (Wilson and Jenkins 1994), we did not try to deconvolve NX Pup C. Another reason is that we got a lower signal-to-noise ratio for NX Pup C.

The first effect of angular anisoplanatism is that the Strehl ratio falls off and the PSF gets wider as the angular distance to the guide star increases: consequently an off-axis PSF will be less sharp. As expected from angular anisoplanatism, the FWHM of NX Pup C is systematically wider than for the calibration source in each JHK filter. Moreover, on the shift-and-add K image, NX PUP C appears elongated in the east-west direction (FWHM 0.18″× 0.27″ in the N-S and E-W directions, respectively, compared to 0.16″× 0.16″ for the on-axis calibration PSF source). This elongation is also observed in the H image but is less significant, and is not seen in the J image.

Such an image elongation can, in principle, result from either angular or temporal anisoplanatism (or both). Angular anisoplanatism would lead to an elongation of the off-axis PSF in the direction of the guide source. This effect has been observed and described by McClure *et al.* (1991). In the case of NX Pup, the expected direction of elongation for NX Pup C would be at a PA of ∼ 45°, i.e. from north-east to south west but not in the east-west direction as observed. Elongation in another direction can be explained by temporal anisoplanatism due to the wind in the dominant turbulent layer (see Roddier *et al.* 1993 and Wilson and Jenkins 1994). The prevalent wind direction at La Silla near the ground is north-south, but we do not know the wind direction in the dominant turbulent layer at the time of our observations. While an off-axis PSF should suffer both effects, the on-axis PSF should show pure temporal anisoplanatism. Yet, the on-axis PSF of the calibration source does not show any significant deviation from circular symmetry. The PSFs of NX Pup A and B computed from the basic blind deconvolution (see above) are quite similar to that of the calibration source. Summing up, neither angular nor temporal anisoplanatism are very likely explanations for the observed elongation of NX Pup C, which may therefore be real. NX Pup C will

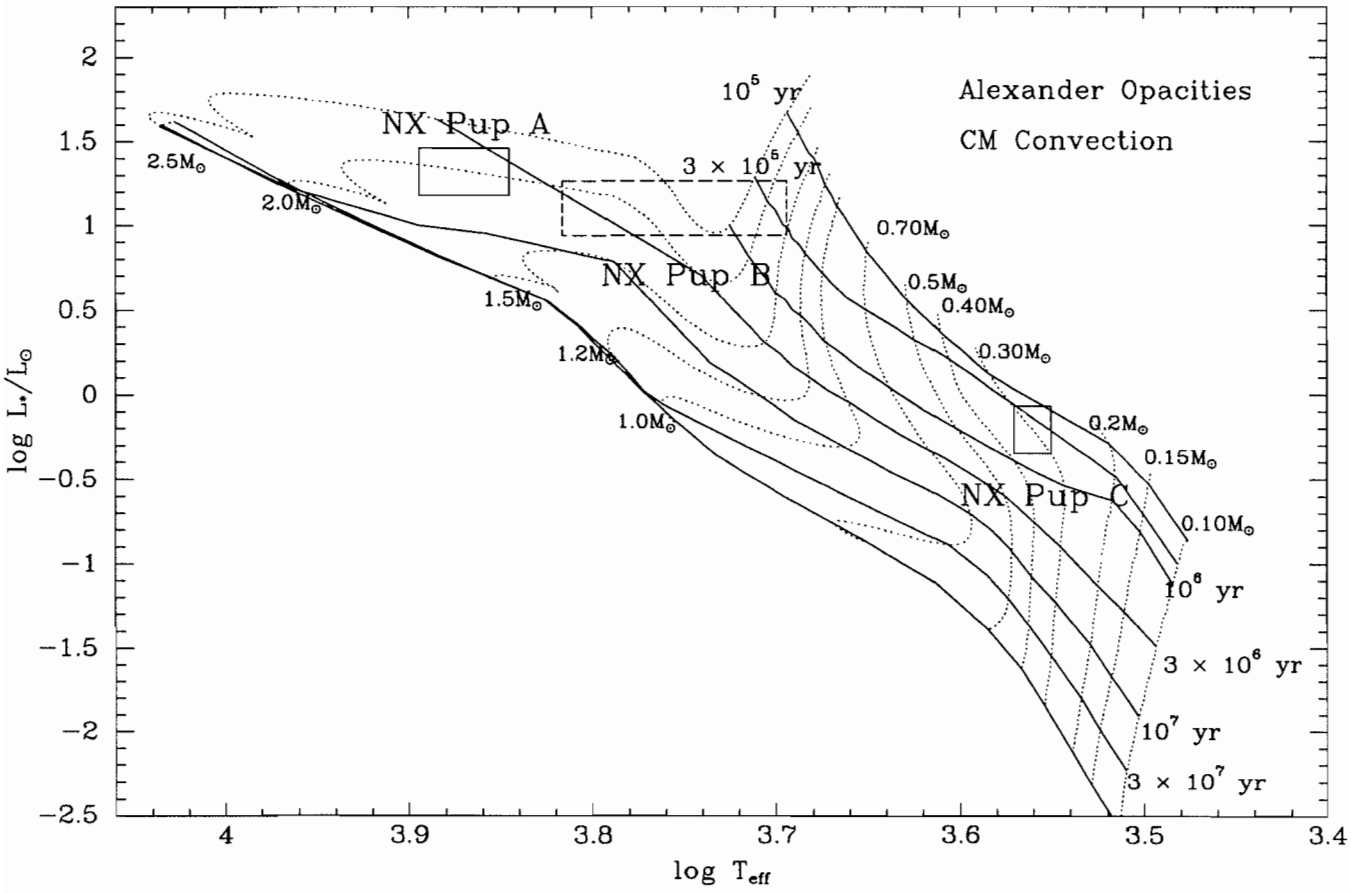

Figure 4: *Position of NX Pup A, B, and C in the HR-Diagram. The pre-main sequence evolutionary tracks are from D'Antona and Mazzitelli (1994). The solid lines represent isochrones and the zero-age main sequence, the dotted lines are the evolutionary tracks for stars in the mass range from 0.1 to 2.5 $M_\odot$. The positions of NX Pup A, B, and C in this diagram are marked by boxes. For NX Pup A we assume a spectral type A7–F2, $V = 10.1^m - 10.5^m$, and $A_V = 0.^m - 0.7^m$ (Blondel and Tjin A Djie 1994). For NX Pup B we assume the same extinction, a spectral type F5–G8 and $V = 10.7^m - 11.1^m$. The evolutionary status of NX Pup C is better defined, yielding an age around 5 × 10^5 yr and a mass of 0.3 $M_\odot$. (From Brandner et al. 1994.)*

TABLE 3. *Equivalent width (in nm) of emission (<0) and absorption (>0) lines in the spectra of NX Pup AB and C (28.1.1994, ESO 1.5-m/ B&C; 20.3.1994, NTT/EMMI).*

NX Pup	AB	C
Hα	double peaked	–2.85
OI 630.0	–0.068	–0.11
Hβ	0.25	–0.58
Hγ	0.53	–0.17
Li I 670.8	–	0.054

TABLE 4. *Evolutionary status of NX Pup A, B, and C.*

NX Pup	A	B	C
Sep.	–	0.128″ ± 0.008″	6.98″ ± 0.04″
PA	–	63.1° ± 3.5°	45.3° ± 0.2°
SpT	A7–F2[1]	F5–G8	M0.5–M1.5
$L/L_\odot$	15–29	9–18	0.45–0.85
Age	5×10^6 yrs	0.3–5 $\times$ 10^6 yrs	5×10^5 yrs

[1] Brand *et al.* 1983, Reipurth 1983, Blondel & Tjin A Djie 1994.

need to be re-observed and at the same time, anisoplanatism should be quantitavely studied.

The Evolutionary Status of the NX Pup System

NX Pup is located at the edge of CG1, a Cometary Globule in the Gum Nebula (see e.g. Henkel 1989, *The Messenger* 57, 8), which is suspected to have been a region of star formation for more than 10^6 years (e.g. Reipurth and Petterson 1993).

NX Pup, a Herbig AeBe star (Irvine 1975) was also resolved as a close binary with a separation of 0.126″ by Bernacca *et al.* (1993) using data from the Fine Guidance Sensor system aboard the Hubble Space Telescope. Thus all previous evolutionary interpretations should be reevaluated as the total observed luminosity in fact comes from at least two stars.

CO+ observations in JHK have easily resolved the NX Pup system, thus allowing us to estimate the flux contribution of each of the components of the system in the infrared. In addition, we used on January 8, 1994 the optical CCD camera at the Danish 1.5-m telescope at La Silla and complemented the IR observations by getting UBVR, Gunn I and Hα photometry for NX Pup AB (unresolved) as well as for NX Pup C that we identify as a low-mass classical T Tauri star. Additional photometric measurements of NX Pup were obtained in the course of the LPTV programme at the Danish 50-cm Strømgren Automatic Telescope (P.S. Thé, private communication, Sterken *et al.* 1995, in preparation).

NX Pup AB and NX Pup C both show a strong excess of Hα emission compared to normal stars included in the same optical images. From the location of these stars in colour-colour J–H vs H–K and V–K vs H–K diagrams we can conclude that NX Pup A belongs to the group of Herbig AeBe stars. All three stars show an intrinsic IR excess. The IR excess is clearly apparent in the spectral energy distributions of the 3 stars plotted in Figure 3.

Spectra of NX Pup C and NX Pup AB were obtained on March 20,1994 with the ESO Multi-Mode Instrument (EMMI) attached to the NTT. Table 3 lists the main features present in the spectra. The presence of the strong Hα emission (EW = 2.85 nm) and the Li I 670.8 nm absorption make NX Pup C a *bona fide* classical T Tauri stars.

Finally, we inferred from these results the luminosity and effective temperature of each star. Figure 4 locates NX Pup A, B, and C in the HR diagram within observational uncertainties. PMS evolutionary tracks from D'Antona and Mazzitelli (1994) are overplotted. Table 4 summarizes the evolutionary status of the NX Pup system. Since the projected distance between NX Pup C and NX Pup AB is 3150 AU, it is likely that NX Pup C is not physically bound to NX Pup AB. On the other hand, we have clear evidence that NX Pup C is a pre-main sequence star. Furthermore it is the only other PMS within a 2.5′ $\times$ 2.5′ field around NX Pup. Therefore, the three stars could quite well form a hierarchical triple system. The identification of NX Pup C as a classical T Tauri star provides the first evidence for low-mass star formation in CG 1.

Acknowledgements

Discussions with C. Jenkins and R. Wilson are gratefully acknowledged. We thank P.S. Thé and C. Sterken for providing us with LPTV measurements prior to publication and A. Tokovinine for providing us some IRAF scripts using DAOPHOT. W. Brandner was supported by a student fellowship of the European Southern Observatory.

References

Brandner W., Bouvier J., Grebel E.K., Tessier E., de Winter D. and Beuzit J.-L., 1994, *A&A* submitted.
Beckers J. M., 1993, *ARAA*, Vol. 31.
Bernacca P.L., Lattanzi M.G., Bucciarelli B., Bastian U., Barbaro G., Pannunzio R., Badiali M., Cardini D., Emanuele A., 1993, *A&A*, **278**, L47.
Blondel P.F.C., Tjin A Djie, H.R.E. 1994, ASP Conf. Ser. 62, 211.
Beuzit J.-L. *et al.*, *The Messenger*, **75**, p. 33.
Brand P.W.J.L., Hawarden T.G., Longmore A.J., Williams P.M., Caldwell J.A.R., 1983, *MNRAS*, **203**, p. 215.
Henkel 1989, *The Messenger*, **57**, p. 8.
Irvine N.J., 1975, *PASP*, **87**, p. 87.
Malbet F., Léna P., Bertout C., 1993, *A&A*, **271**, L9.
Mc Lure R.D., Arnaud J., Murray Fletcher J., Nieto J. and Racine R., 1991, *PASP*, **103**, p. 570-575.
Reipurth B., 1983, *A&A*, **117**, p. 183.
Reipurth B., Pettersson B., 1993, *A&A*, **267**, p. 439.
Rigaut F., Rousset G., Kern P., Fontanella J.-C., Gaffard J.P., Merkle F., Léna P., 1991, *A&A*, **250**, p. 280.
Roddier F., Northcott M.J., Graves J.E., McKenna D.L., Roddier D., 1993, *J. Opt. Soc. Am. A*, Vol. 10, p. 957.-965
Sterken *et al.* 1995, in preparation.
Tessier E., 1993, Thesis, University of Paris 6.
Tessier E., Bouvier J., Lacombe F., 1994, *A&A*, **283**, p. 827.
Wilson R. and Jenkins C., 1994, *MNRAS* in preparation.